ACS Sustainable Chemistry & Engineering

Research Article

pubs.acs.org/journal/ascecg

Dehydrated Sucrose Nanoparticles as Spacers for Graphene–Ionic Liquid Supercapacitor Electrodes

David J. Bozym,[†] Sibel Korkut,[‡] Michael A. Pope,[†] and Ilhan A. Aksay*[,†]

[†]Department of Chemical and Biological Engineering, Princeton University, Princeton, New Jersey 08544, United States

[‡]Vorbeck Princeton Research Center, Vorbeck Materials Corporation, 11 Deerpark Drive #203, Monmouth Junction, New Jersey 08852, United States

Supporting Information

ABSTRACT: The addition of dehydrated sucrose nanoparticles increases the gravimetric capacitance of electrochemical double-layer capacitor electrodes produced via the evaporative consolidation of graphene oxide–water–ionic liquid gels by more than two-fold. Dehydrated sucrose adsorbs onto graphene oxide and serves as a spacer, preventing the graphene oxide from restacking during solvent evaporation. Despite 61 wt % of the solids being electrochemically inactive dehydrated sucrose nanoparticles, the best electrodes achieved an energy density of ∼13.3 Wh/kg, accounting for the total mass of all electrode components.

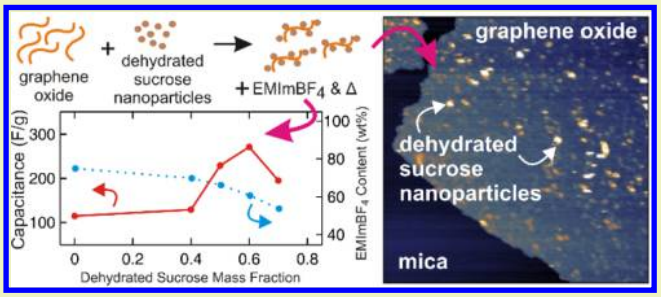

KEYWORDS: *Supercapacitor, Spacer, Sucrose, Room-temperature ionic liquid, Energy density*

INTRODUCTION

One of the routes for enhancing the performance of current electrochemical double-layer capacitors (EDLCs), also known as supercapacitors, involves designing new electrodes with commonly available materials with higher gravimetric capacitance (C_G). Thus, materials with a large specific surface area (SSA) and a high intrinsic double-layer capacitance (C_{DL}) are needed, because C_G is the product of SSA and C_{DL}. Carbonaceous materials such as activated carbon,[1] carbon black,[2] carbon nanotubes,[3] and graphene-based materials[4−8] have been favored as active materials for EDLC electrodes as they are electrically conductive and feature large SSAs, typically greater than 1000 m^2/g. Of these materials, functionalized graphene sheets (FGSs), a class of materials produced via the thermal reduction and exfoliation of graphite oxide (GO)[9,10] or the chemical reduction of graphene oxide,[11] i.e., FGS_2, where the subscript represents the atomic carbon:oxygen ratio (C:O), are promising for electrodes with high gravimetric capacitance. FGSs boast an exceptionally large theoretical surface area of up to 2630 m^2/g and have recently been shown to exhibit a C_{DL} up to 4 times greater than that of pristine graphene because of their high density of residual functional groups and defects.[12−14]

However, one of the greatest challenges in reaching the potential performance of FGS-based EDLCs is processing the FGSs in a way to maintain their large SSA.[15] Aside from wrinkles and surface defects,[9] FGSs do not contain an intrinsic, rigid porous structure like other carbonaceous materials, most notably activated carbon.[16] Consequently, the SSA of a bulk FGS-based electrode is exclusively dependent on how the FGSs aggregate upon being processed into dense electrodes. Typically, FGS-based electrodes are processed from dispersions of FGSs in an appropriate solvent. The SSA of FGSs can be large when well-dispersed in suspension (∼1740 m^2/g).[17] Upon solvent evaporation, however, capillary and van der Waals forces cause the sheets to collapse and restack, drastically reducing the SSA of the bulk film (∼390 m^2/g).[18,19] The reduction in SSA is even more pronounced (<1 m^2/g) for FGS_2 given the material lacks intrinsic wrinkles.

There are two approaches to prevent the restacking of FGSs: (i) physically altering the morphology of the FGSs[6,20−22] and (ii) adding a second nano-sized particle to serve as an inter-sheet spacer.[8,18,23,24] The addition of a secondary component to serve as an inter-sheet spacer for FGSs is a more promising route as the spacing of the FGSs can be controlled by changing the size of the added spacer. The disadvantage of this approach, however, is the negative influence of the extra weight of the spacer on the energy density of the device (E), which is directly proportional to the mass fraction of the active electrode material (f) as shown in Eq 1:

$$E = \frac{f}{8} C_G U^2 \quad (1)$$

where U is the applied voltage. Therefore, in such a system, the challenge is to prevent the restacking of FGSs while keeping the energy density high. A possible route to accomplishing this goal is to use nano-scale spacers that are also active materials.

So far, solid components such as metal and ceramic nanoparticles,[23,25,26] small molecules,[24,27] polymers,[28,29] carbon

Received: August 25, 2016

DOI: 10.1021/acssuschemeng.6b02050
ACS Sustainable Chem. Eng. XXXX, XXX, XXX−XXX

Table 1. EDLC Performance Metrics of Graphene-Based Electrodes Employing Various Solid Spacer Materials

Spacer material	Electrolyte	C_G (F/g)	w_s[a]	E^*[b] (Wh/kg)	E (Wh/kg)
dehydrated sucrose (this work)	$EMImBF_4$	271	0.6	89 (3 V)	13.3 (3 V)
tin nanoparticles[25]	2 M KNO_3	320	nr[d]	36[c]	nr[d]
carbon nanotubes[18]	30 wt % KOH	318	0.5	3.9	nr[d]
carbon nanotubes[18]	30 wt % KOH	224	0.11	6.6	nr[d]
carbon nanotubes[30]	1 M KCl	290.6	0.5	10	nr[d]
carbon nanotubes[30]	1 M $TEABF_4$/PC	201.0	0.5	62.8 (3 V)	nr[d]
carbon nanotubes[30]	EMImTFSI	280	0.5	155.6 (4 V)	nr[d]
p-phenyldiamine[27]	1 M H_2SO_4	282.3	nr[d]	28	nr[d]
platinum nanoparticles[23]	"acid"	269	~0.5	nr[d]	nr[d]
$CaCO_3$ nanoparticles[26]	2 M KCl	240	~0.12	nr[d]	nr[d]
carbon black[31]	$TEABF_4$ in AN	218	0.1	43.6	nr[d]
melamine resin[24]	1 M $LiPF_6$ in EC/DEC	210	nr[d]	28	nr[d]
poly(ionic liquid)[28]	EMImTFSI	187	nr[d]	6.5 (3.5 V)	nr[d]
carbon black[32]	6 M KOH	138	0.76	5	nr[d]
carbon black[32]	1 M $LiPF_6$ in EC/DEC	83.2	0.76	26	nr[d]

[a]Weight percent of solids from the spacer material. [b]Reported without considering the mass of the electrolyte ($f = 1$). [c]Calculated using the term $^1/_2 C_G U^2$. [d]Not reported.

nanotubes,[18,30] and carbon blacks[31,32] have been used as spacers between FGSs. All of these studies report high C_G, as shown in Table 1, yet they neglect to include the weight of the spacer material, the weight of the electrolyte, or both in the calculation of E. Hence, they report an E that is exaggerated as it is based solely on the weight of the active solid materials.

In this study, we use nanoparticles produced via the dehydration of sucrose, a renewable feedstock, as spacers between FGSs, as the density of dehydrated sucrose (DS) is expected to be much lower than that of a metal- or oxide-based nanoparticle of equal size, thereby minimizing the increase in the total weight of the electrode. Using an evaporative consolidation procedure developed by our group,[33] we combine these hydrophilic DS nanoparticles with an aqueous suspension of FGS_2 and water-soluble ionic liquid (IL) and consolidate the suspension into electrodes that are heat treated to reduce the FGS_2 into conductive FGSs. We show that including DS prevents the restacking of FGSs effectively and increases the C_G from 115 to 330 F/g (reported per gram of FGS). Moreover, with this approach, surprisingly high energy densities (13.3 Wh/kg) can be achieved despite the large amounts of DS (60 wt % solids) used within the electrodes. While this is not the best energy density reported for FGS-based electrodes, it is an impressive value given that the electrodes have not been optimized for other processing parameters and that the DS is expected to be electrochemically inactive. Further improvements are anticipated by rendering DS conductive and electrochemically active through heat treatments and subsequent optimization of the processing parameters.

EXPERIMENTAL SECTION

Material Preparation. *Graphite Oxide (GO).* GO was produced by an improved Hummers method according to a procedure described previously.[34] Briefly, 3 g of graphite (Asbury 3061) was added to 360 mL of concentrated H_2SO_4 and 40 mL of concentrated H_3PO_4 in a 1 L glass beaker with a polytetrafluoroethylene (PTFE) stir bar. Eighteen grams of $KMnO_4$ was added, and the temperature was held at 45 °C for 16 h. The reaction mixture was poured over 400 g of ice, and 6 mL of 35 wt % H_2O_2 was added. The resulting GO was washed with water (2×), 35 wt % HCl (3×), and anhydrous ethanol (3×). The GO was stored in ethanol in a slurry form until it was used.

Dehydrated Sucrose. DS was synthesized according to an acid-catalyzed dehydration of sucrose adapted from ref 35. Briefly, 3 g of a saturated aqueous solution of sucrose (2.0 g of sucrose/mL of water) was added to a scintillation vial with a PTFE stir bar. Two milliliters of concentrated H_2SO_4 was added dropwise from a PTFE-stoppered glass syringe (inner diameter of 10.3 mm) at a rate of 0.25 mL/min under vigorous stirring. The reaction mixture was then quickly diluted in 40 mL of deionized (DI) water and stirred for an additional 30 s. Finally, two aliquots of 3 mL of 0.5 g/mL NaOH were pipetted sequentially into the mixture. The mixture was distributed into 3.5 kDa dialysis membranes and dialyzed for 10 days against DI water that was exchanged daily.

Electrode Fabrication, Characterization, and Testing. 1-Ethyl-3-methylimidazolium tetrafluoroborate ($EMImBF_4$, Sigma-Aldrich) was purchased at a purity of >99 % and used as received. The procedure for electrode preparation is based on modifications to the evaporative consolidation approach developed by Pope et al.[33] Aqueous suspensions of FGS_2 and DS were prepared at various FGS_2:DS (mass ratios) by tip sonication for 15 min at 40 % amplitude. The total solid content was adjusted to 8 mg/mL by evaporating the excess solvent. Two batches of electrodes were prepared, each differing in how the total $EMImBF_4$ content was maintained. Electrodes termed "electrolyte-lean" were prepared with an FGS_2:$EMImBF_4$ of 70:30; "electrolyte-rich" electrodes were prepared by mixing the total solids (graphene oxide and DS) with the IL in a 70:30 ratio. To facilitate mixing, IL was diluted with DI water to a ratio of 1:5. After addition of IL, the prepared suspensions were stirred overnight and then drop-cast onto platinum pucks (1.5 cm diameter, 99.9 % purity) such that a total loading of 1.5 mg of FGS_2 was achieved. The electrodes were left to dry overnight. The consolidated electrodes were placed in an ashing furnace and heat treated in a nitrogen-blanketed atmosphere to 300 °C (ramp rate of 20 °C/min), after which the furnace was turned off and the electrodes were left to cool to room temperature.

The mass of the thermally reduced DS−FGS−$EMImBF_4$ electrodes was determined by weighing the electrode after heat treatment and subtracting the mass of the platinum puck. To calculate the solids loading post-heat treatment, a sacrificial electrode was analyzed using thermogravimetric analysis (TGA) by heating the films to 500 °C (beyond the decomposition of $EMImBF_4$) and determining the residual mass of the electrode film. The mass of FGS on each electrode was determined by first multiplying the total mass of the reduced film by the mass fraction of the total solid material determined by TGA and then by multiplying the result by the mass fraction of FGS in the solids, based on the initial FGS_2:DS ratio. The average mass of FGS after heat treatment was ~0.5 mg. Electrochemical testing of the electrodes was performed using a spring-loaded stainless steel test cell (MTI Corp.) in a two-electrode configuration using a Celgard 3501

DOI: 10.1021/acssuschemeng.6b02050
ACS Sustainable Chem. Eng. XXXX, XXX, XXX−XXX

membrane separator presoaked in $EMImBF_4$. All devices were assembled in an argon-filled (99.9999 %, AirGas) glovebox (Innovative Technology). Cyclic voltammetry and electrochemical impedance spectroscopy (EIS) were performed using a computer-controlled potentiostat (VSP, Bio-Logic). C_G was calculated from the cyclic voltammetry data using the following equation:

$$C_G = 2\frac{i_{avg}}{\upsilon m} \quad (2)$$

where i_{avg} is the average of the absolute anodic and cathodic currents at the midpoint of the cyclic voltammogram (CV), υ is the scan rate, and m is the average mass of FGS on both electrodes. The CVs were collected over a 3.0 V window. The impedance measurements were taken at open circuit potential over a frequency range from 200 kHz to 10 mHz with a sinus perturbation of 10 mV. Measurements were taken at 10 % of one period of oscillation.

Additional Characterization. The C:O values of the materials before and after heat treatment were determined by energy dispersive X-ray spectroscopy (EDS). X-ray diffraction (XRD) was performed on FGS−DS composites using a desktop diffractometer (Rigaku MiniFlex II) with a Cu Kα radiation source (λ = 0.154 nm). The d_{0002} spacing is calculated using Bragg's law. Atomic force microscopy (AFM) was performed in contact mode and in a liquid cell (LC) using a MultiMode atomic force microscope with a Nanoscope IIIa controller and an FC-type contact-mode liquid cell (Veeco Instruments). AFM samples were prepared by drop-casting FGS_2 suspensions onto a freshly cleaved mica substrate. LC−AFM measurements were performed in the presence of an aqueous DS suspension (0.25 mg/mL). Raman spectroscopy (Horiba Raman spectrophotometer, λ = 523 nm) was performed on pressed pellets of GO and FGS as well as DS pucks produced by drop-casting concentrated suspensions onto a PTFE substrate.

RESULTS AND DISCUSSION

We first present the performance data for the EDLC electrodes to show that the addition of DS can effectively increase the C_G of the electrode. Next, we use LC−AFM and XRD to show that the DS nanoparticles adsorb onto FGS_2 in an aqueous environment and that the d_{0002} spacing of consolidated FGS_2-DS increases with an increasing DS content. We provide additional material characterization after heat treatment and electrochemical impedance measurements to further probe the electronic and ionic transport in the materials. Lastly, high-temperature heat treatment data are presented to show that the DS may be converted to an active electrode component and garner further improvements in device performance if higher heat treatment temperatures could be reached during electrode processing.

Electrode Performance. The composite electrodes have three components: FGS, DS, and $EMImBF_4$. To assess the impact of each component on the C_G, as shown in Figure 1, we compare (i) electrolyte-lean electrodes for which the $EMImBF_4$ content was maintained at an FGS_2:$EMImBF_4$ of 70:30 and (ii) electrolyte-rich electrodes for which the solids (FGS_2 and DS):$EMImBF_4$ of 70:30 was maintained, as the initial mass fraction of DS in the solid component of the electrode (w_{DS}) is varied. Here, we assume that DS particles do not contribute to the capacitance of the electrode, and hence report C_G based on the weight of FGSs only. This assumption will be supported by the characterization data for DS nanoparticles, which will be presented below. The CVs used to calculate the C_G of each electrode are largely rectangular within the voltage window and do not show a significant contribution from Faradaic redox peaks (Figure 1a). Therefore, we do not expect any significant contribution from pseudocapacitance to the capacitance values either.

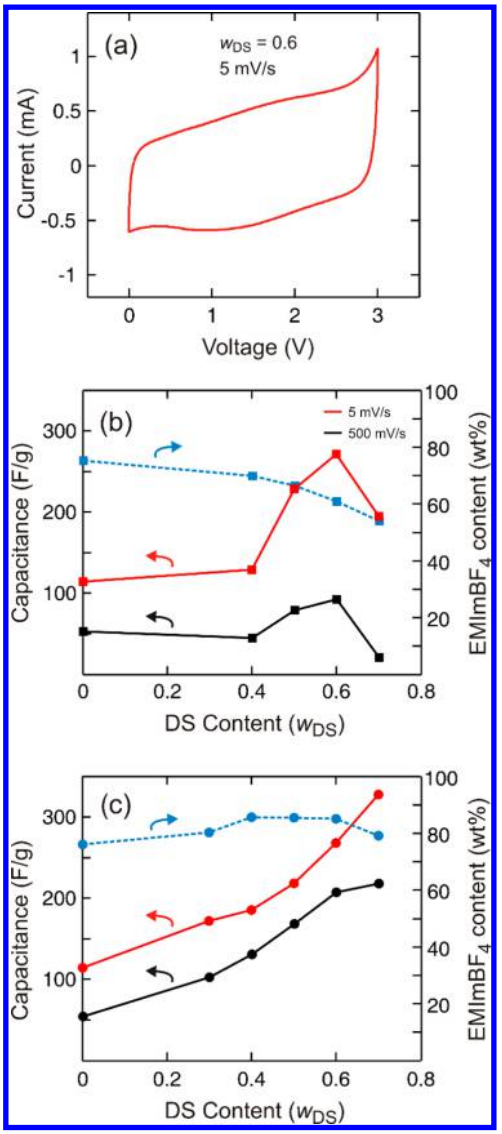

Figure 1. (a) Representative cyclic voltammogram of an electrolyte-lean electrode with a w_{DS} of 0.6. Gravimetric capacitance and total $EMImBF_4$ content of (b) electrolyte-lean and (c) electrolyte-rich electrodes as a function of DS content. Capacitance data are reported per gram of FGS after heat treatment.

Figure 1b shows that the C_G for electrolyte-lean electrodes at 5 mV/s remains approximately constant up to a w_{DS} of 0.4. At a w_{DS} of 0.5, C_G increases and upon further addition of DS nanoparticles reaches a maximal value of 271 F/g at a w_{DS} of 0.6, which is more than double that achieved by the control electrodes (w_{DS} = 0). This maximum is achieved despite having an $EMImBF_4$ content (61 wt %) lower than that of the control electrodes (75 wt %). Increasing w_{DS} beyond 0.6 resulted in a decrease in C_G. A similar trend in C_G is observed for the electrolyte-lean electrodes at a high scan rate of 500 mV/s; however, the absolute values are significantly lower at this high rate especially at a w_{DS} of 0.6, where the C_G is less than one-third of that at 5 mV/s. As shown in Figure 1c, the C_G of the electrolyte-rich electrodes increases with an increasing DS content reaching a value of 330 F/g at a w_{DS} of 0.7 at 5 mV/s. Additionally, the high rate performance of the electrolyte-rich electrodes is significantly better than that of the electrolyte-lean electrodes for all DS contents. The improved rate performance

DOI: 10.1021/acssuschemeng.6b02050
ACS Sustainable Chem. Eng. XXXX, XXX, XXX−XXX

of the electrolyte-rich electrodes suggests that the decrease in C_G for the electrolyte-lean electrodes beyond a w_{DS} of 0.6 may be attributed to the smaller fraction of $EMImBF_4$.

Figure 2 shows E calculated using Eq 1 using all of the capacitance results obtained. Though improvements in C_G are

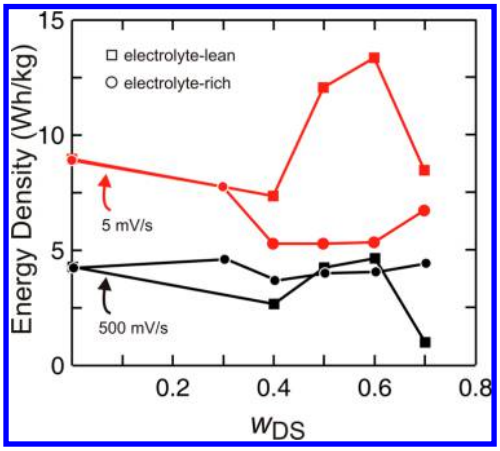

Figure 2. Calculated energy density of the electrolyte-lean and electrolyte-rich electrodes reported per total mass of the electrode (FGS, DS, and $EMImBF_4$).

reported for both batches of electrodes, improvements in E are seen for only the electrolyte-lean electrodes, as E depends on the total mass of all components (i.e., FGS, DS, and $EMImBF_4$). At 5 mV/s, the electrolyte-lean case reaches a maximum E of ~13.3 Wh/kg when w_{DS} = 0.6. In the absence of any improvements to the capacitance, the E would have been 62 % of that of the control electrode based on the decrease in f. However, the improvements in C_G lead to an E that is 148 % of the E for the control electrode. On the other hand, despite reaching a similarly high C_G, the electrolyte-rich case cannot achieve an E of >5 Wh/kg. This difference is almost exclusively the result of the higher $EMImBF_4$ content in the electrolyte-rich electrodes, which effectively lowers f. Additionally, the E for both batches of electrodes at 500 mV/s is similar, suggesting that the gains in C_G afforded at 500 mV/s do not compensate for the additional mass in the electrode.

To investigate whether DS contributed to the capacitance of the electrodes, cyclic voltammetry measurements on the 300 °C reduced DS nanoparticles were attempted. However, as the resulting electrodes were not robust and not adherent to the current collector in the presence of an electrolyte, the measurements could not be performed. The absence of a coherent film also prevented the measurement of the electrical conductivity of DS directly. While we will later provide evidence through use of other characterization methods, such as Raman spectroscopy and elemental analysis, that DS nanoparticles are not electronically conducting, the values for E reported in Figure 2 are not affected regardless of the electrical conductivity of DS, as the mass of the DS was accounted for in the value of f for the E calculation.

DS as Spacers for FGS_2. We have used LC–AFM to gain further insight into the interactions between DS and FGS and explain the observed improvements in C_G and E. Figure 3a shows an FGS_2 on a mica surface with DS particles selectively adsorbed onto the sheet. The AFM data demonstrate that the DS nanoparticles are adsorbed to and uniformly dispersed on the FGS_2. This approach, compared to transmission electron microscopy, eliminates the uncertainties associated with sample

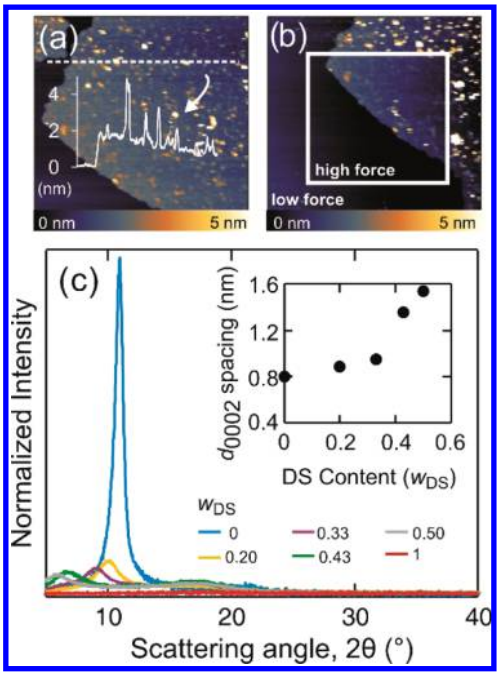

Figure 3. (a) LC–AFM of DS on FGS_2 (b) High- and low-force contact-mode scans showing the removal of DS from the FGS_2 under high force. (c) XRD spectra of FGS_2–DS films drop-cast from suspension.

preparation that can cause non-adsorbed particles to deposit on FGS_2 during the dispersion casting procedure. As the height profile shows, the roughness is on the order of the average heights of the DS nanoparticles [0.5–2.5 nm (Figure S1)]. Furthermore, Figure 3b shows that the DS can be removed from the FGS_2 by applying a high force to the cantilever tip. As both FGS_2 and DS contain acidic functional groups (Figure S2), both materials are expected to be negatively charged in water and, hence, are expected to repel one another. However, as the acidic functional groups are thought to be concentrated at the edges of FGS_2,[36] the electrostatic repulsion between DS nanoparticles and FGS_2 may be weak on the plane of FGS_2. We attribute the adsorption of DS onto FGS_2 to weak interactions, including van der Waals forces and hydrogen bonding between the oxygen-containing functional groups on both DS and FGS_2. This hypothesis is further supported by the selectivity of adsorption, shown in Figure 3b: the DS adsorbs onto FGS_2 but does not adsorb onto the underlying mica substrate. Adsorption may also occur at lattice vacancy sites on the FGS_2;[37] however, there is little evidence to suggest that these sites exist in significant amounts on FGS_2. These results confirm that DS is indeed acting as a spacer by specifically adsorbing on the FGS_2.

We performed XRD on films of FGS_2 and DS drop-cast from aqueous suspensions to determine how the DS content affects the spacing of FGS_2 after solvent evaporation. Figure 3c presents the signal intensity of the films as a function of scattering angle (2θ). The signal intensity was normalized on the basis of the total FGS_2 content, such that the degree of restacking could be compared across all samples. For a w_{DS} of 0, a sharp peak is observed at 10.1°, which corresponds to a d_{0002} of 0.8 nm, a spacing similar to that for stacked graphene oxide.[34] When w_{DS} increases to 0.2, the peak shifts to a smaller scattering angle, signifying that the d_{0002} spacing of FGS_2 has increased. Also, the original peak at 10.1° is absent, which

DOI: 10.1021/acssuschemeng.6b02050
ACS Sustainable Chem. Eng. XXXX, XXX, XXX–XXX

suggests that this DS content is sufficient to completely disrupt the regular stacking of the FGS_2 sheets. Furthermore, the signal intensity at a w_{DS} of 0.2 is less than one-tenth of that measured at a w_{DS} of 0. As the DS content increases, the peak continues to shift toward smaller scattering angles. This could be due to the increased elastic energy requirement for bending the FGS_2 as the DS particles move closer to one another.[38] The d_{0002} spacing reaches 1.54 nm at a w_{DS} of 0.5, which is almost double the d_{0002} spacing of graphite oxide. It is interesting to note that the spacing between FGS_2 increases at a greater rate (i.e., larger slope) above a w_{DS} of ~0.4. Paralleling this transition in the d_{0002} spacing, the C_G does not improve appreciably until w_{DS} is greater than 0.4 for the electrolyte-lean electrodes. The w_{DS} for the transition differs slightly between the C_G and d_{0002} spacing data, potentially because of the addition of the room-temperature IL and the heat treatment in the actual electrodes. Nevertheless, the similarity in the trend suggests that the reason for the lack of improvement in C_G at a w_{DS} of <0.4 is likely the insufficient spacing between the FGSs.

Material and Electrode Characterization after Heat Treatment. Figure 4 shows Raman spectroscopy results for both FGS_2 and DS before and after they had been heated to 300 °C. Prior to heat treatment, FGS_2 exhibits two prominent peaks, the D- and G-peaks. The D-peak near 1350 cm^{-1} is the result of the breathing mode of six-membered aromatic rings that is observed only in the presence of defects that disrupt these aromatic domains, while the G-peak at 1580 cm^{-1} represents the in-plane oscillations of any sp^2 carbon bonds.[39] The Raman spectrum for DS is notably different as both the D- and G-peaks are absent. This result illustrates a key structural difference between FGS and DS: while remnants of the planar, honeycomb lattice of graphene remain in FGS_2, this organized structure is not present in DS. After heat treatment, the DS spectrum still lacks a D-peak, but a small G-peak can be observed, suggesting that only isolated sp^2 pairs but no full aromatic domains have formed. Both the D- and G-peaks are still present in thermally reduced FGS_2. The inset of Figure 4 shows that the C:O values are quite different before and after heat treatment. While the C:O of FGS increases from 2.0 (i.e., FGS_2) to 5.1, the C:O of DS after heat treatment is only 3.0. Both the absence of sp^2 domains and the high oxygen content (~25 atom %) lead us to assume that DS is likely electrically insulating and therefore does not serve as a significant electronic material or provide a significant capacitive contribution in the electrode at the investigated processing temperature. For this reason, the C_G values in Figure 1 were reported in terms of the mass of FGS only. On the other hand, the C_G value for the electrolyte-rich electrodes at a high DS content (w_{DS} = 0.7) is exceptionally high, leading one to question whether DS reduction is significantly influenced by the presence of $EMImBF_4$ to the point where DS begins to serve as an active electrode component. Protic ionic liquids and aprotic ionic liquids with transition metal catalysts have been shown to convert sucrose into hydroxymethylfurfural, a precursor of carbonaceous materials;[40,41] however, $EMImBF_4$ alone has not been shown to catalyze the reaction. Traditionally, sucrose-based materials require a high-temperature calcination (>550 °C) to generate an electrochemically active carbonaceous material.[42−44] However, in our study, DS was reduced at only 300 °C, because of the limitations imposed by the volatility and thermal stability of $EMImBF_4$,[33] which is subjected to the same heat treatment protocol as DS during the electrode fabrication process. To improve C_G further, we attempted to heat treat the DS and then mix it with FGSs; however, during this process, the particles aggregated irreversibly. While developing an approach for incorporating an electrically conductive form of DS into our FGS electrodes may result in significant improvements, devising such a process is far from trivial and would require an independent investigation.

To further investigate the ionic and electronic transport mechanisms in the various electrodes, we performed EIS. Figure 5 shows Nyquist plots for the two batches of electrodes

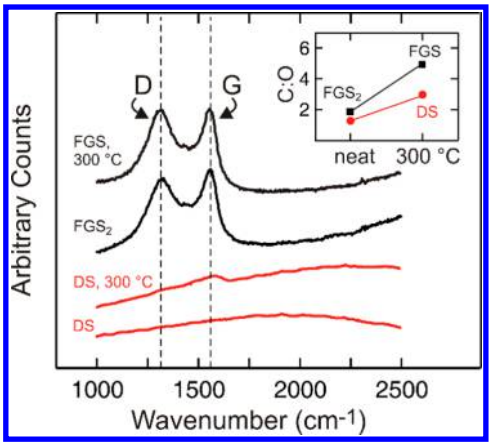

Figure 4. Raman spectra of FGS_2 and DS before and after heat treatment. C:O is shown in the inset.

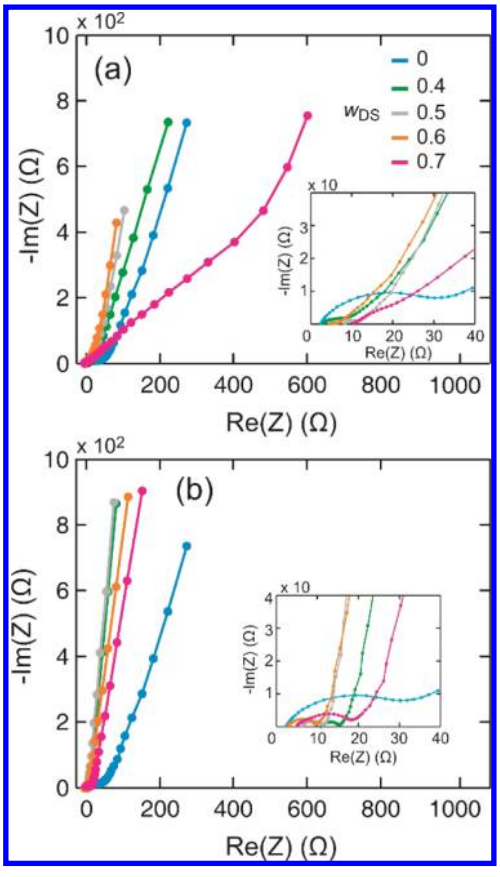

Figure 5. Nyquist plots of the (a) electrolyte-lean and (b) electrolyte-rich electrodes along with selected views of the high-frequency regions.

DOI: 10.1021/acssuschemeng.6b02050
ACS Sustainable Chem. Eng. XXXX, XXX, XXX−XXX

previously studied. For the electrolyte-lean electrodes, the slopes of the low-frequency range for w_{DS} of 0 and 0.4 are nearly identical, indicating similar ionic transport behavior in these electrodes. At a w_{DS} of 0.5, the slope increases, suggesting an improvement in the level of ionic transport despite a decrease in $EMImBF_4$ content and supporting the claim that at a w_{DS} of >0.4, the improvement in C_G is due to the better accessibility of FGSs by the $EMImBF_4$ ions. However, at a w_{DS} of 0.7, the slope of the mid-frequency range clearly follows a 45° line, which indicates a Warburg-like impedance associated with ionic transport in porous electrodes. This result provides evidence of our previous claim that the C_G of the electrolyte-lean electrode for a w_{DS} of 0.7 was low because of an insufficient amount of $EMImBF_4$ per total mass of solids in the electrode. Comparatively, as seen in Figure 5b for the electrolyte-rich electrodes, the slope of the low-frequency range increases significantly more at a w_{DS} of 0.4, likely because of the excess $EMImBF_4$ in the electrode. Upon further addition of DS, the slope begins to decrease as it approaches a w_{DS} of 0.7. At this DS content, the total $EMImBF_4$ content with respect to the mass of FGS is approximately 93 wt %, which is a significant excess based on previous reports. Though we expect the ionic conductivity not to be limiting at exceptionally high $EMImBF_4$ content, the $EMImBF_4$ may interfere with the electronic conductivity of the FGS network by swelling the composite and increasing the electronic resistance between the sheets.

We further investigate this hypothesis by analyzing the high-frequency impedance data. In comparing the high-frequency responses of the two batches of electrodes, we note several differences. The semicircles of the electrolyte-lean electrodes formed at high frequencies shown in the inset of Figure 5a have diameters smaller than those of the electrolyte-rich electrodes for corresponding DS contents shown in the inset of Figure 5b. Additionally, the slopes of the mid-frequency regime for the electrolyte-rich electrodes are larger than those of the electrolyte-lean electrodes. The relatively smaller semicircles of the electrolyte-lean electrodes suggest that the electronic resistance of these electrodes is smaller than that of the electrolyte-rich electrodes. This again supports the idea that the presence of more $EMImBF_4$ most likely swells the conductive network and increases the electronic resistance in the case of electrolyte-rich electrodes. Surprisingly, the semicircles for the DS-containing electrodes are smaller than those for the electrodes without DS. This appears to be counterintuitive as one may not predict the electronic conductivity to increase upon addition of an insulating spacer. However, we suspect that the difference may arise from the relatively easier tunneling of electrons through DS compared to that through $EMImBF_4$ because of the differences in their dielectric constant. Alternatively, the structure of the percolated FGS network may be changing substantially in the presence of DS, leading to the changes in the observed conductivity. Further detailed characterization is needed to investigate these hypotheses to improve our understanding of the effect of the components on the electronic resistance of the electrode.

The EDLC electrodes fabricated during this work were stable over the course of electrochemical testing. We did not observe significant degradation in the capacitance of our electrodes during our testing protocol, which consists of approximately 30 cycles. Though extensive testing of cycle life stability is one consideration in the design of EDLCs, the aim of this study is to demonstrate the proof of concept that nanoscale spacers can be used to improve the E of electrodes processed via evaporative consolidation.

High-Temperature Heat Treatment of DS. On the basis of the previous analysis, the value of w_{DS} in the electrodes indicates the fraction of the total solid content, which, in addition to the total $EMImBF_4$ content, contributes to f. However, if the DS could be converted into an active carbonaceous material, its mass will now increase f and also contribute to the reported C_G. One way to convert DS to an active material is to heat it to higher temperatures. Figure 6a shows Raman spectroscopy for DS heat treated to temperatures higher than 300 °C. At 500 °C, the Raman spectrum for DS features prominent D- and G-peaks indicating the presence of a network of sp^2 bonds. The C:O of this material was measured via EDS to be 5 ± 1, which is comparable to the C:O of the FGS material in our electrodes, as previously reported. Upon extreme heat treatment to 1200 °C, the peaks become sharper and the material reaches a high C:O of 22 ± 4. Additionally, the G' peak near 2700 cm^{-1}, which is characteristic of graphite, begins to emerge at higher temperatures. Figure 6b shows the corresponding DSC and TGA data of DS as a function of heat treatment temperature. At low temperatures, the broad endotherm is likely the result of the removal of residual water, which accounts for approximately 5 % of the total mass of the sample. A significant chemical change likely occurs around 200 °C as evidenced by an appreciable mass loss (38 %) and a sharp exotherm. At temperatures above 300 °C, subsequent mass loss is observed, and at high temperatures,

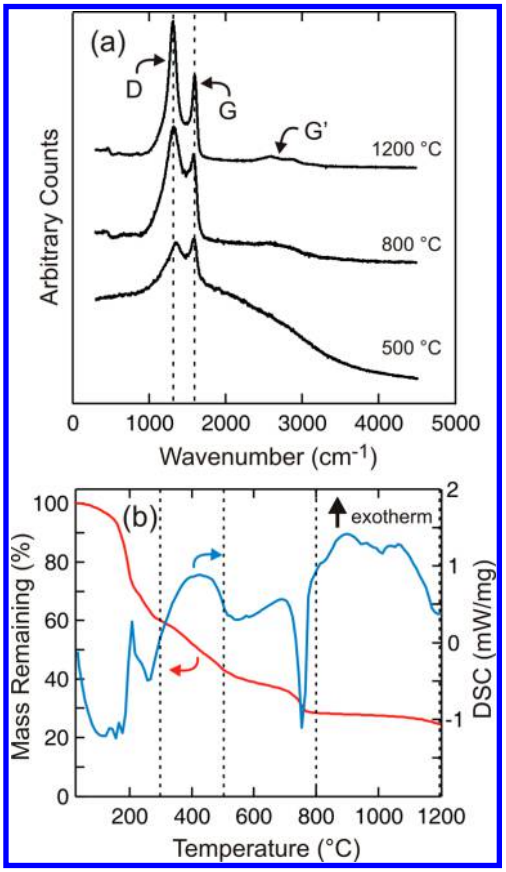

Figure 6. (a) Raman spectra of DS heated in an inert atmosphere from 500 to 1200 °C. (b) DSC and TGA data of DS heated to 1200 °C under an inert atmosphere at a ramp rate of 20 °C/min.

DOI: 10.1021/acssuschemeng.6b02050
ACS Sustainable Chem. Eng. XXXX, XXX, XXX−XXX

the mass loss of DS is substantial: at 500 °C only 45 wt % of the material remains. This mass loss may significantly affect the density as well as the mechanical properties of the DS.

As stated above, currently, we cannot process our electrodes at temperatures much higher than 300 °C, as we find that $EMImBF_4$ at these temperatures evaporates or decomposes and, hence, the IL content is difficult to control. To capture the full benefits of this material in an EDLC electrode, either electrolytes (e.g., ILs or solid-state electrolytes) with decomposition temperatures greater than 500 °C will need to be used in the evaporative consolidation approach, or a modified electrode fabrication approach during which the IL is not exposed to the same temperatures as DS will need to be established.

CONCLUSIONS

DS nanoparticles synthesized via a hydrothermal reduction of sucrose were used as spacers to prevent FGS_2 from restacking to a GO-like structure during EDLC electrode assembly. We showed that DS adsorbs directly onto FGS_2 in an aqueous environment and provides a physical barrier to intersheet collapse due to van der Waals and capillary forces during solvent evaporation. We coupled the aqueous suspensions of DS-decorated FGS_2 with a water-miscible IL to fabricate EC electrodes using a scalable, one-pot procedure. The resulting electrodes exhibited a significantly improved C_G, more than double that of the control electrode in the best cases. If we account for the total mass of the electrode, the best electrodes achieved an E of 13.3 Wh/kg despite containing 23 wt % inactive spacer material and 61 wt % $EMImBF_4$. This is the highest E of an electrode using a solid spacer material reported to date for FGS-based electrodes. Though the scan rate dependence of the electrodes improves with the addition of excess $EMImBF_4$, the gains in C_G do not compensate for the decrease in f incurred by the added mass of the electrolyte. Future efforts to transform the DS into a conductive electrode component may offer additional improvements in f and provide further insight into the design of highly energy-dense EDLC electrodes.

ASSOCIATED CONTENT

Supporting Information

The Supporting Information is available free of charge on the ACS Publications website at DOI: 10.1021/acssuschemeng.6b02050.

Height profiles of DS nanoparticles, C:O values of neat and heat-treated DS nanoparticles as a function of time, and FTIR data of neat and heat-treated DS nanoparticles (PDF)

AUTHOR INFORMATION

Corresponding Author

*E-mail: iaksay@princeton.edu.

Notes

The authors declare the following competing financial interest(s): S.K., M.A.P., and I.A.A. declare a financial interest in Vorbeck Materials Corp. that manufactures functionalized graphene under the trade name Vor-x.

ACKNOWLEDGMENTS

This work was supported in part by Pacific Northwest National Laboratory (operated for the U.S. Department of Energy by Battelle) via Grant DE-AC05-76RL0183. S.K. was supported in part by the Army Research Laboratory (DOD) SBIR under Contract W9111QX-11-C-0079. M.A.P. acknowledges additional support from an Army Research Office (ARO)/Multidisciplinary Research Initiative (MURI) under Grant W911NF-09-1-0476.

REFERENCES

(1) Qu, D.; Shi, H. Studies of Activated Carbons Used in Double-Layer Capacitors. *J. Power Sources* **1998**, *74*, 99−107.
(2) Beck, F.; Dolata, M.; Grivei, E.; Probst, N. Electrochemical Supercapacitors Based on Industrial Carbon Blacks in Aqueous H_2SO_4. *J. Appl. Electrochem.* **2001**, *31*, 845−853.
(3) Niu, C.; Sichel, E. K.; Hoch, R.; Moy, D.; Tennent, H. High Power Electrochemical Capacitors Based on Carbon Nanotube Electrodes. *Appl. Phys. Lett.* **1997**, *70*, 1480−1482.
(4) Zhu, Y.; Murali, S.; Stoller, M. D.; Ganesh, K. J.; Cai, W.; Ferreira, P. J.; Pirkle, A.; Wallace, R. M.; Cychosz, K. A.; Thommes, M.; et al. Carbon-Based Supercapacitors Produced by Activation of Graphene. *Science* **2011**, *332*, 1537−1541.
(5) Wang, Y.; Shi, Z.; Huang, Y.; Ma, Y.; Wang, C.; Chen, M.; Chen, Y. Supercapacitor Devices Based on Graphene Materials. *J. Phys. Chem. C* **2009**, *113*, 13103−13107.
(6) Liu, C. G.; Yu, Z. N.; Neff, D.; Zhamu, A.; Jang, B. Z. Graphene-Based Supercapacitor with an Ultrahigh Energy Density. *Nano Lett.* **2010**, *10*, 4863−4868.
(7) Stoller, M. D.; Park, S. J.; Zhu, Y. W.; An, J. H.; Ruoff, R. S. Graphene-Based Ultracapacitors. *Nano Lett.* **2008**, *8*, 3498−3502.
(8) Yang, X.; Cheng, C.; Wang, Y.; Qiu, L.; Li, D. Liquid-Mediated Dense Integration of Graphene Materials for Compact Capacitive Energy Storage. *Science* **2013**, *341*, 534−537.
(9) Schniepp, H. C.; Li, J.-L.; McAllister, M. J.; Sai, H.; Herrera-Alonso, M.; Adamson, D. H.; Prud'homme, R. K.; Car, R.; Saville, D. A.; Aksay, I. A. Functionalized Single Graphene Sheets Derived from Splitting Graphite Oxide. *J. Phys. Chem. B* **2006**, *110*, 8535−8539.
(10) McAllister, M. J.; Li, J.-L.; Adamson, D. H.; Schniepp, H. C.; Abdala, A. A.; Liu, J.; Herrera-Alonso, M.; Milius, D. L.; Car, R.; Prud'homme, R. K.; et al. Single Sheet Functionalized Graphene by Oxidation and Thermal Expansion of Graphite. *Chem. Mater.* **2007**, *19*, 4396−4404.
(11) Stankovich, S.; Dikin, D. A.; Piner, R. D.; Kohlhaas, K. A.; Kleinhammes, A.; Jia, Y.; Wu, Y.; Nguyen, S. T.; Ruoff, R. S. Synthesis of Graphene-Based Nanosheets via Chemical Reduction of Exfoliated Graphite Oxide. *Carbon* **2007**, *45*, 1558−1565.
(12) Peigney, A.; Laurent, C.; Flahaut, E.; Bacsa, R. R.; Rousset, A. Specific Surface Area of Carbon Nanotubes and Bundles of Carbon Nanotubes. *Carbon* **2001**, *39*, 507−514.
(13) Pope, M. A.; Punckt, C.; Aksay, I. A. Intrinsic Capacitance and Redox Activity of Functionalized Graphene Sheets. *J. Phys. Chem. C* **2011**, *115*, 20326−20334.
(14) Pope, M. A.; Aksay, I. A. Four-Fold Increase in the Intrinsic Capacitance of Graphene through Functionalization and Lattice Disorder. *J. Phys. Chem. C* **2015**, *119*, 20369−20378.
(15) Punckt, C.; Pope, M. A.; Liu, J.; Lin, Y.; Aksay, I. A. Electrochemical Performance of Graphene as Effected by Electrode Porosity and Graphene Functionalization. *Electroanalysis* **2010**, *22*, 2834−2841.
(16) Laine, J.; Yunes, S. Effect of the Preparation Method on the Pore Size Distribution of Activated Carbon from Coconut Shell. *Carbon* **1992**, *30*, 601−604.
(17) Pope, M. A. Electrochemical Double-Layer Capacitors Based on Functionalized Graphene. Ph.D. Thesis, Princeton University, Princeton, NJ, 2013.
(18) Wang, Y.; Wu, Y.; Huang, Y.; Zhang, F.; Yang, X.; Ma, Y.; Chen, Y. Preventing Graphene Sheets from Restacking for High-Capacitance Performance. *J. Phys. Chem. C* **2011**, *115*, 23192−23197.
(19) Scherer, G. W. Theory of Drying. *J. Am. Ceram. Soc.* **1990**, *73*, 3−14.

DOI: 10.1021/acssuschemeng.6b02050
ACS Sustainable Chem. Eng. XXXX, XXX, XXX−XXX

(20) Luo, J.; Jang, H. D.; Sun, T.; Xiao, L.; He, Z.; Katsoulidis, A. P.; Kanatzidis, M. G.; Gibson, J. M.; Huang, J. Compression and Aggregation-Resistant Particles of Crumpled Soft Sheets. *ACS Nano* **2011**, *5*, 8943−8949.
(21) Yan, J.; Liu, J.; Fan, Z.; Wei, T.; Zhang, L. High-Performance Supercapacitor Electrodes Based on Highly Corrugated Graphene Sheets. *Carbon* **2012**, *50*, 2179−2188.
(22) Liu, F.; Song, S.; Xue, D.; Zhang, H. Folded Structured Graphene Paper for High Performance Electrode Materials. *Adv. Mater.* **2012**, *24*, 1089−1094.
(23) Si, Y.; Samulski, E. T. Exfoliated Graphene Separated by Platinum Nanoparticles. *Chem. Mater.* **2008**, *20*, 6792−6797.
(24) Lee, J. H.; Park, N.; Kim, B. G.; Jung, D. S.; Im, K.; Hur, J.; Choi, J. W. Restacking-Inhibited 3D Reduced Graphene Oxide for High Performance Supercapacitor Electrodes. *ACS Nano* **2013**, *7*, 9366−9374.
(25) Qin, Z.; Li, Z. J.; Zhang, M.; Yang, B. C.; Outlaw, R. A. Sn Nanoparticles Grown on Graphene for Enhanced Electrochemical Properties. *J. Power Sources* **2012**, *217*, 303−308.
(26) Salgado, S.; Pu, L.; Maheshwari, V. Targeting Chemical Morphology of Graphene Oxide for Self-Assembly and Subsequent Templating of Nanoparticles: A Composite Approaching Capacitance Limits in Graphene. *J. Phys. Chem. C* **2012**, *116*, 12124−12130.
(27) Sk, M. M.; Yue, C. Y. Layer-by-layer (LBL) Assembly of Graphene with p-Phenylenediamine (PPD) Spacer for High Performance Supercapacitor Applications. *RSC Adv.* **2014**, *4*, 19908−19915.
(28) Kim, T. Y.; Lee, H. W.; Stoller, M.; Dreyer, D. R.; Bielawski, C. W.; Ruoff, R. S.; Suh, K. S. High-Performance Supercapacitors Based on Poly(ionic liquid)-Modified Graphene Electrodes. *ACS Nano* **2011**, *5*, 436−442.
(29) Korkut, S.; Roy-Mayhew, J. D.; Dabbs, D. M.; Milius, D. L.; Aksay, I. A. High Surface Area Tapes Produced with Functionalized Graphene. *ACS Nano* **2011**, *5*, 5214−5222.
(30) Cheng, Q.; Tang, J.; Ma, J.; Zhang, H.; Shinya, N.; Qin, L.-C. Graphene and Carbon Nanotube Composite Electrodes for Supercapacitors with Ultra-High Energy Density. *Phys. Chem. Chem. Phys.* **2011**, *13*, 17615−17624.
(31) Wang, M.; Oh, J.; Ghosh, T.; Hong, S.; Nam, G.; Hwang, T.; Nam, J.-D. An Interleaved Porous Laminate Composed of Reduced Graphene Oxide Sheets and Carbon Black Spacers by In Situ Electrophoretic Deposition. *RSC Adv.* **2014**, *4*, 3284−3292.
(32) Wang, G.; Sun, X.; Lu, F.; Sun, H.; Yu, M.; Jiang, W.; Liu, C.; Lian, J. Flexible Pillared Graphene-Paper Electrodes for High-Performance Electrochemical Supercapacitors. *Small* **2012**, *8*, 452−459.
(33) Pope, M. A.; Korkut, S.; Punckt, C.; Aksay, I. A. Supercapacitor Electrodes Produced through Evaporative Consolidation of Graphene Oxide-Water-Ionic Liquid Gels. *J. Electrochem. Soc.* **2013**, *160*, A1653−A1660.
(34) Marcano, D. C.; Kosynkin, D. V.; Berlin, J. M.; Sinitskii, A.; Sun, Z.; Slesarev, A.; Alemany, L. B.; Lu, W.; Tour, J. M. Improved Synthesis of Graphene Oxide. *ACS Nano* **2010**, *4*, 4806−4814.
(35) Zhang, J.; Shen, W.; Pan, D.; Zhang, Z.; Fang, Y.; Wu, M. Controlled Synthesis of Green and Blue Luminescent Carbon Nanoparticles with High Yields by the Carbonization of Sucrose. *New J. Chem.* **2010**, *34*, 591−593.
(36) Lerf, A.; He, H.; Forster, M.; Klinowski, J. Structure of Graphite Oxide Revisited. *J. Phys. Chem. B* **1998**, *102*, 4477−4482.
(37) Dimiev, A.; Kosynkin, D. V.; Alemany, L. B.; Chaguine, P.; Tour, J. M. Pristine Graphite Oxide. *J. Am. Chem. Soc.* **2012**, *134*, 2815−2822.
(38) Lu, Q.; Arroyo, M.; Huang, R. Elastic Bending Modulus of Monolayer Graphene. *J. Phys. D: Appl. Phys.* **2009**, *42*, 102002.
(39) Ferrari, A. C.; Robertson, J. Interpretation of Raman Spectra of Disordered and Amorphous Carbon. *Phys. Rev. B: Condens. Matter Mater. Phys.* **2000**, *61*, 14095−14107.
(40) Moreau, C.; Finiels, A.; Vanoye, L. Dehydration of Fructose and Sucrose into 5-Hydroxymethylfurfural in the Presence of 1-H-3-Methyl Imidazolium Chloride Acting Both as Solvent and Catalyst. *J. Mol. Catal. A: Chem.* **2006**, *253*, 165−169.
(41) Chun, J.-A.; Lee, J.-W.; Yi, Y.-B.; Hong, S.-S.; Chung, C.-H. Catalytic Production of Hydroxymethylfurfural from Sucrose using 1-Methyl-3-Octylimidazolium Chloride Ionic Liquid. *Korean J. Chem. Eng.* **2010**, *27*, 930−935.
(42) Wei, L.; Yushin, G. Electrical Double Layer Capacitors with Sucrose Derived Carbon Electrodes in Ionic Liquid Electrolytes. *J. Power Sources* **2011**, *196*, 4072−4079.
(43) Zhang, L.; Zhang, F.; Yang, X.; Long, G.; Wu, Y.; Zhang, T.; Leng, K.; Huang, Y.; Ma, Y.; Yu, A.; Chen, Y. Porous 3D graphene-based bulk materials with exceptional high surface area and excellent conductivity for supercapacitors. *Sci. Rep.* **2013**, *3*, 1408.
(44) Wu, X.-L.; Wen, T.; Guo, H.-L.; Yang, S.; Wang, X.; Xu, A.-W. Biomass-Derived Sponge-like Carbonaceous Hydrogels and Aerogels for Supercapacitors. *ACS Nano* **2013**, *7*, 3589−3597.

DOI: 10.1021/acssuschemeng.6b02050
ACS Sustainable Chem. Eng. XXXX, XXX, XXX−XXX